MDPI

*Article*

# Simulating the Effect of Depositing an 8YSZ Buffer Layer in P92/Al$_2$O$_3$ on the Thermal Cycles Endurance and Fracture Toughness of the System

**Kezhi Huang** [1,2,3,†]**, Yu Liu** [1,2,4,†]**, Weijing Wang** [1,2,3]**, Qinghe Yu** [1,2,3,4,*]**, Jing Mi** [1,2]**, Lei Hao** [1,2,3]**, Hao Liu** [1,2]**, Baolong Yuan** [1,2]**, Wei Xiao** [2]**, Xiaotao Chen** [5]**, Ziqiang Dong** [6,*]** and Ping Wang** [7]

[1] National Engineering Research Center of Nonferrous Metals Materials and Products for New Energy, GRINM Group Co., Ltd., Beijing 100088, China; hkzchihaya@gmail.com (K.H.); liuyu@grinm.com (Y.L.)
[2] GRIMAT Engineering Institute Co., Ltd., Beijing 101407, China
[3] General Research Institute for Nonferrous Metals, Beijing 100088, China
[4] GRINM (GuangDong) Institute for Advanced Materials and Technology, Foshan 528051, China
[5] Shipbuilding Industry Co., Ltd., Dalian 116021, China
[6] Materials Genome Institutes, Shanghai University, Shanghai 200444, China
[7] Zouping Hengjia New Material Technology Co., Ltd., Binzhou 256200, China
[*] Correspondence: author: yuqh@grinm.com (Q.Y.); zqdong@shu.edu.cn (Z.D.)
[†] These authors contributed equally to this work.

**Abstract:** The effect of depositing 8YSZ between serving as an intermediate layer of the P92/Al$_2$O$_3$ was analyzed via finite element analysis. The result shows that depositing an 8YSZ buffer coat beneath the Al$_2$O$_3$ will dramatically decrease the maximum principal stress in the coating system in thermal shock. The stress intensity factor, $K_I$, and J-integral are also decreased which indicates the crack propagation resistance is improved. Inserting a 100 nm 8YSZ buffer layer could reduce the $K_I$ and J-integral by 2 orders of magnitude. Thus, cracks are less likely to initiate and propagate. Moreover, coating an 8YSZ layer between the P92/Al$_2$O$_3$ can significantly change the stress distribution pattern in the Al$_2$O$_3$ coating. The 8YSZ with a proper coefficient of thermal expansion between that of the Al$_2$O$_3$ and P92 and good deformability is an ideal buffer layer to improve the thermal cycle endurance and prolong the service life of the Al$_2$O$_3$ coating.

**Keywords:** ultra-supercritical power plant; protective coating; buffer layers; finite element analysis; thermal stress

## 1. Introduction

Coal is increasingly demanded as a power source and it is expected that by the year 2030, coal consumption will exceed 6000 million tons of carbon equivalent and contribute to 42% of the electricity supply worldwide according to International Energy Agency [1]. A large percentage of carbon dioxide emissions would result from the coal burning in power plants, leading to severe global warming problems [2]. Therefore, there is an urgent request to reduce carbon dioxide emissions. Increasing the efficiency of the steam power plants is urgently required and can be achieved by operating with a super-critical or ultra-supercritical working medium [3]. The efficiency of an ultra-supercritical plant (e.g., 300 bar and 630 °C) can reach over 48%, while that of a subcritical plant (below 220.6 bar and 374 °C) is below 35% [4]. The ultra-supercritical power plant is more efficient and environmentally friendly compared to the traditional coal-burning power plant and has been widely put into service. However, the extreme working condition in the plant requires components with high corrosion resistance in presence of the water vapor and CO$_2$. Many kinds of materials have been developed to construct facilities that could withstand high pressure and temperature in the long term [5]. Among them, Ferritic-martensitic P92 was chosen in the steam pipes, headers, and superheater of many facilities for application at up to 650 °C

because of its high strength, low expansion coefficient, high oxidation resistance in ultra-supercritical steam, and excellent creeping resistance [6–9]. But for long-term service, $Al_2O_3$ protective coating is needed to prolong the service life. Research on the creep behavior of the P92 shows that under 650 °C, the P92 welded joints can only withstand about $10^4$ h operation, while the P92 base metal can survive about $10^5$ h [9]. Preparing a protective coating, especially on the welded joint is an ideal option to prolong the service life or increase the service temperature of components. $Al_2O_3$ is an excellent candidate for this application due to its high strength, good corrosion resistance, and thermal stability in the presence of water vapor [10–15]. B.A. Pint conducted a long-term performance experiment of aluminide-coated T91 and 304 L SS. The result shows that, compared to the uncoated specimen, the alumina-forming coating could successfully prevent the accelerated attack of the substrate in humid air at 650–800 °C [16]. However, little research was conducted about the optimization of the coating preparation and nano-thick $Al_2O_3$ coating in this specific application. For long-term service of $Al_2O_3$ coating, the most critical problem is the huge thermal mismatch of the coating and the substrate. However, the huge thermal mismatch of the $Al_2O_3$ and P92 could result in residual stress during the operation of the plant. It could result in tremendous thermal residual stress, causing crack initiation and the final failure of the coating when the coating-substrate system experiences thermal cycles during the operation of the power plant. Preparing a double or multiple-layer system is a solution to the problem [17]. Preparing an 8YSZ intermediate transient layer with intermediate thermal expansion performance between the $Al_2O_3$ coating and the substrate and good high-temperature endurance can be a way to reduce the thermal residual stress of the coating and prolong its lifespan [18,19]. However, little research analyzes the improvement of fracture resistance by introducing the buffer layer, which is somewhat similar to the notch effect of the fatigue behavior of materials [20]. In this paper, simulations of the P92/$Al_2O_3$ and P92/8YSZ/$Al_2O_3$ were conducted to investigate the effect of preparing a nano-thick intermediate coat beneath the $Al_2O_3$. The effect of the buffer layer on the reduction of the thermal stress and improvement of the thermal cycle endurance of the coating-substrate system was analyzed by finite element analysis. The result was also verified by experiment. This work is a preliminary work to find the relationship between the topcoat and the thermal stress of the nano-thick composite coating and the preparation and optimization of protective $Al_2O_3$ on the P92 steel in an ultra-supercritical power plant.

## 2. Material and Methods

The simulation of the stress field of the coating system under thermal cycles was conducted using the commercial software ANSYS 19. Per our previous experimental study, the coating specimens were all annealed in a vacuum tube furnace for 2 h at 700 °C to eliminate any residual stress that existed after magnetron coating [21]. All models were set in a stress-free state at 700 °C which is slightly higher than the operation temperatures of the ultra-supercritical condition (650 °C). The maximum principal stress was considered the major factor that impacted the thermal cycle endurance of the coating as both the $Al_2O_3$ and $Y_2O_3$ coatings are brittle and fragile. Moreover, a pre-meshed crack fracture analysis was also conducted to evaluate the fracture resistance of the composite of the P92/8YSZ/$Al_2O_3$ coating system.

The thermal shock experiment was carried out on the P92/$Al_2O_3$ and P92/8YSZ/$Al_2O_3$ specimens prepared by radio-frequency magnetron sputtering methods, details of which were similar to our previous study [22] to verify the calculation result.

### 2.1. Analytic Model

The detail of constructing the analytic model for the finite-element analysis has been described in our previous study [23]. In ANSYS, interpolation functions were used to calculate the strain and stress increment of each element. The software transforms those mechanical equilibrium equations into simultaneous equations.

By Applying Hooke's law and the principle of virtual work, and considering the load vector $\{\Delta F\}$ only includes the thermal force, the thermal stress can be derived as follows:

$$\{\Delta F\}_T^e = \iiint \{B\}^T \{D\}\{B\}\{\alpha\}dxdydz \tag{1}$$

where $\{B\}$ is the strain matrix, $\{D\}$ is the elastic matrix of the given material which is determined by the elastic modulus ($E$), and Poisson's ratio ($\nu$.), $\alpha$ is the thermal expansion coefficient.

The fracture analysis considers the Model-I stress intensity factor (SIF-1) and the J-Integral which are associated with the crack resistance of a given material.

The stress intensity factor $K_I$ of a given crack-like flaw is determined as follows:

$$K_I = \sigma Y \sqrt{\pi a} \tag{2}$$

where $\sigma$ is the applied stress, $a$ is the radius of the flaw, and $Y$ is the geometry factor that represents the geometry of the flaw [24].

The critical stress intensity factor $K_{IC}$ of a given material can be calculated as follows:

$$\text{the } K_{IC} = \left[ \frac{EG}{(1-\nu)^2} \right]^{1/2} \tag{3}$$

where $E$ and $\nu$ are Young's modulus and Poisson's ratio of the coating material, respectively. $G$ is the energy release rate of the crack during mechanical equilibrium cracking [25].

The J-integral represents the energy intensity of the fracture area in the material, which is defined as follows:

$$J = \int_r \left( W{\cdot}dy - T{\cdot}\frac{\partial u}{\partial x}ds \right) \tag{4}$$

where $W$ is the strain energy density and $T = n\sigma$ is a traction vector pointing outward, $n$ is a unit normal vector and $\sigma$ is the stress. $ds$ is the counterclockwise increment of the fracture area [26].

For ideal elastic material, the J-integral is linked to the stress intensity factor, which fulfills:

$$J = K^2/E' \tag{5}$$

where $E'$ is elastic modulus. For plane stress condition the $E' = E$, and $E$ is the Young's modulus. For a plane strain condition $E' = E/\left(1-\nu^2\right)$, the critical J-integral, $J_k$, can be derived if $K_{IC}$ is substituted in the equation [27].

When $K_I > K_{IC}$, or $J > J_k$, an existing crack can propagate and cause failure. Thus, for a pre-cracked specimen under certain thermal cycles, the smaller the $K_I$ or $J$, the less likely the crack would propagate and cause failure, and thus the better the thermal shock endurance for the materials [28].

### 2.2. Model Geometry and Material Properties

The composite coating was fabricated on a P92 steel using a radio-frequency magnetron sputtering method. The morphology of the composite coating is shown in Figure 1. It could be seen that the composite coating is dense and homogeneous. The interface between the coating layer and substrate was smooth. No obvious defects were presented before the thermal shock experiments.

The model constructed in the finite element analysis consists of two parts. One part is the P92/8YSZ/Al$_2$O$_3$ composite coating system as shown in Figure 2. The thickness of the top alumina layer is 150 nm. The thickness of the 8YSZ interlayer is $t$. The other model is a cylinder shape. The P92 steel cylinder is 1 mm in diameter and 0.5 mm in thickness. All parts are uniform and homogenous. As a result, 2-dimensional axisymmetric models were carried out to simplify the analysis. The property values that were incorporated into the simulation are listed in Table 1.
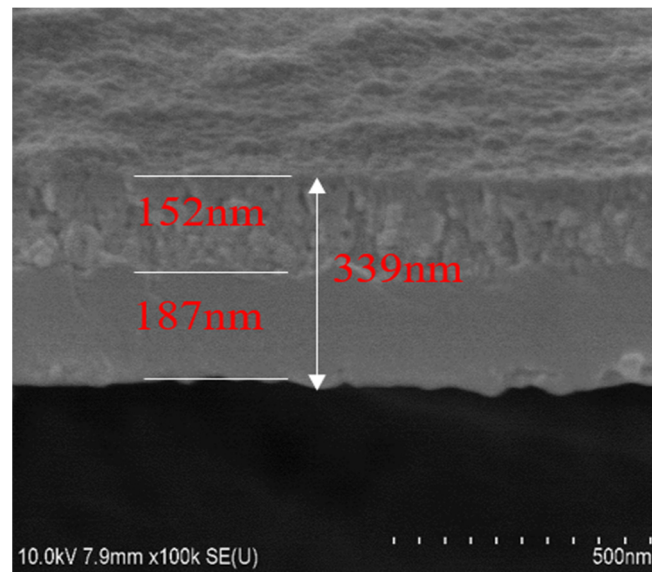
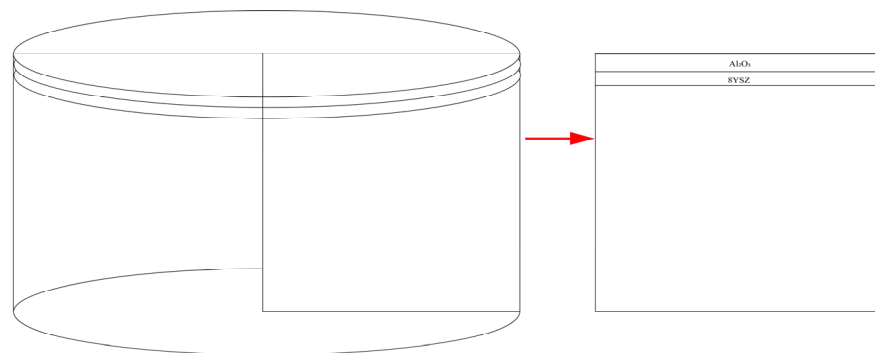**Figure 1.** SEM images of the nano-thick coatings.



**Figure 2.** The geometry of the model.

**Table 1.** Properties of the coating and the substrate (temperature is 25 °C if not noted).

| Materials | Young's Modulus (GPa) | Poisson's Ratio | Coefficient of Thermal Expansion ($10^{-6}$ $K^{-1}$) |
|---|---|---|---|
| P92 | 125 [10] | 0.3 [10] | 11.5 (100 °C) [6] |
| $\alpha$-$Al_2O_3$ | 370 [14] | 0.22 [14] | 8.8 [14] |
| 8YSZ | 48 [24] | 0.1 [24] | 1.04 [24] |

### 2.3. Meshing

In order to construct nano-thick models with adequate size for meshing, a micronmeter was set as the standard unit of length. All related property values were converted to a similar unit. For example, the Young's modulus of the P92 steel is set to 0.2 N/μm$^3$. A nano-thick model that is large enough and could properly mesh with an adequate number of elements was built. The element of the coating was set as a square with 25 nm side length. While the elements of the substrate were quadrilaterals with edge lengths varied from 25 nm to 50 μm. The total number of elements for all models is approximately 400,000.

### 2.4. Boundary Condition and Load

Static structural analysis was chosen to simulate the stress field. Frictionless support constraints were applied to the left edge and the bottom edge of the model to prevent any translation of each edge along its normal direction. The bond constraint was applied to each

contact pair to prevent any relative tangential translation on the interfaces between them. In other words, all nodes of the contact surfaces will not change their relative positions. Those nodes located at the same point at the initial stage will always contact together. The temperature considered in the simulation increases linearly from 25 °C to 700 °C. Under this circumstance, the top coating would more likely peel off from the surface. The mesh, loading, and boundary conditions of the finite element modeling are shown in Figure 3.
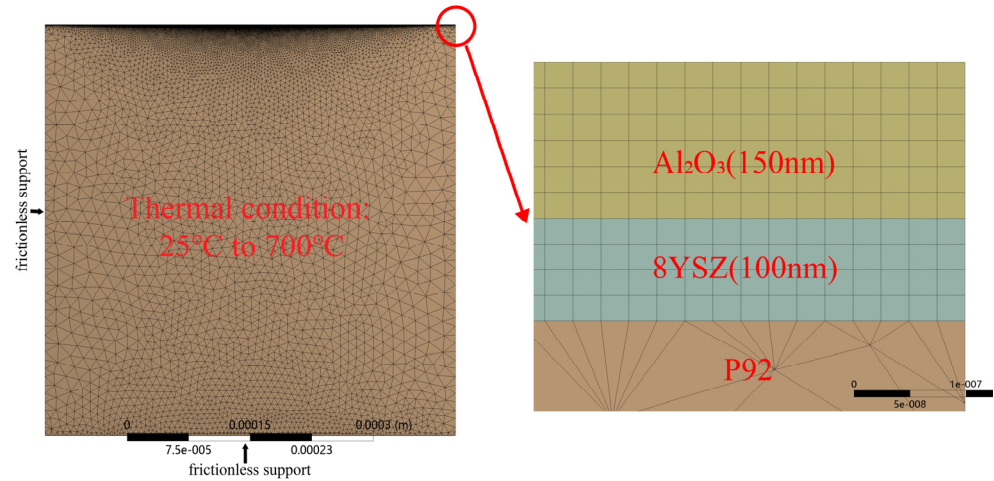


**Figure 3.** Mesh and boundary conditions of the finite element.

*2.5. Fracture Toughness Analysis*

Pre-meshed crack analysis was applied to analyze the fracture toughness of the composite coating system. As shown in Figure 4, a 250 nm-long crack with a depth of 0.5% of the total depth of the coating was placed into the coating model where the highest stress was present and hence the crack was most likely to initiate and propagate. The crack tip was placed right in the nodal at the interface. The origin of the coordinate system for carrying out the crack propagation simulation is anchored at the edge of the interface with the X-axis pointing inwards leading to the crack growing direction.
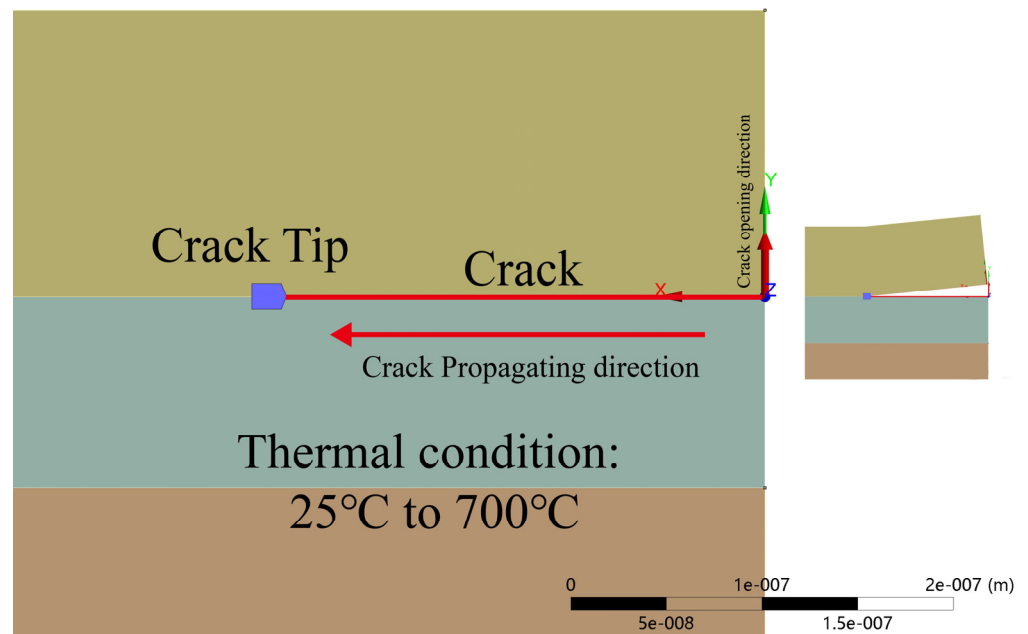


**Figure 4.** The pre-mesh crack of the finite element.

## 3. Result and Discussion

The stress fields of single-layer $Al_2O_3$ (150 nm) coating and $8YSZ/Al_2O_3$ (150 nm) nano-thick composite coatings with different thicknesses of 8YSZ interlayers cooling from 700 °C to 25 °C were analyzed. As shown in Figure 5, the max principal stress decreases abruptly from 862 MPa to 256 MPa when 50 nm of the YSZ layer is introduced between the P92 and $Al_2O_3$. Then, the max principle stress increases evidently from 250 MPa to about 450 MPa when the thickness of YSZ changes from 50 nm to 100 nm. The further thickness increase of the YSZ layer causes an insignificant rise of the max principle stress and a stress plateau at around 500 MPa appears when the thickness of the YSZ layer increases further from 100 nm to 150 nm. The result indicates that introducing an 8YSZ buffer layer into the $P92/Al_2O_3$ coating can greatly reduce the max principal stress owing to its intermediate CTE and good deformability due to its relatively low Young's modulus and Poisson's ratio. The shear stress of the coating system decreases slightly from 453 MPa to 431 MPa when the 8YSZ layer with a thickness of 50 nm is placed between the P92 substrate and alumina layer. With the further thickness increase of the 8YSZ layer, the shear stress increases slightly and gradually levels at 500 MPa, which should be caused by the accumulation of the plastic deformation along the circumferential direction of the thicker 8YSZ could result in more stress along the same direction. The max Mises stress remains almost the same at around 850 MPa when the thickness of the 8YSZ interlayer increases, indicating that inserting an 8YSZ interlayer into the $P92/Al_2O_3$ imposes an insignificant effect on the total stress or strain if all 3 axes were taken into consideration. Thus, before a crack is initiated, the elastic behavior of the $8YSZ/Al_2O_3$ composite coating and the monolayer $Al_2O_3$ coating would be roughly the same.
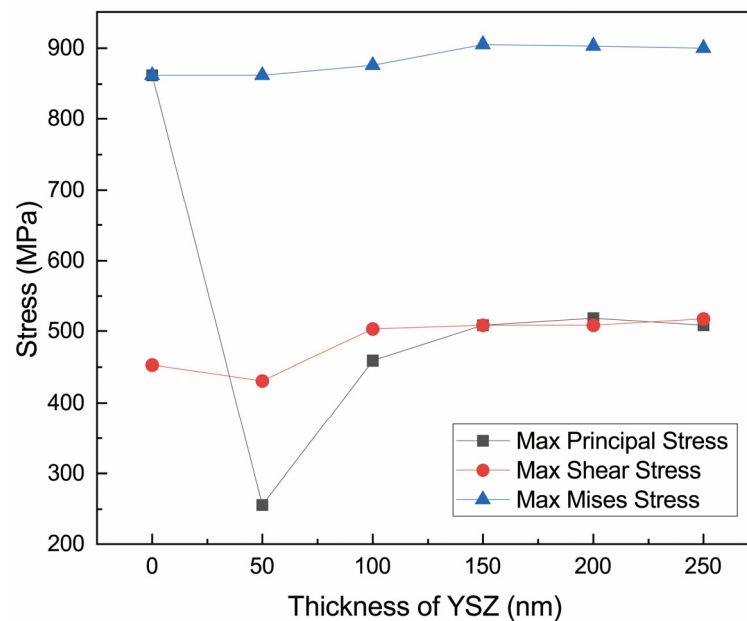


**Figure 5.** Effect of thickness of 8YSZ interlayer on the stress of the coating system.

The thermal stress developed in the coating system can be described using the stress singularity theory. The sudden stiffness change at the coating interfaces creates the stress singular point at the edge of the interfaces. When the coating is very thin, and the stress singular region is small, the thermal residual stress at the edge, $\sigma_p$, can be calculated as follows:

$$\sigma_p = \frac{K}{r^\lambda}, \; r < r_0 \tag{6}$$

where $r_0$ is the vicinity zone of the stress singularity and $K$ is the stress intensity factor. Both $K$ and $\lambda$ are determined by Poisson's ratio, Young's modulus, and the contact angles of the two layers. When the coating thickness is small, the stress singularity zone enlarges

with the increase of the coating thickness which reduces the $\lambda$. Hence, the $\sigma_p$ at the stress singularity zone also increases with the decrease of $\lambda$ [29].

The max principal stress fields of the single-layer $Al_2O_3$ coating and the $8YSZ/Al_2O_3$ composite coatings are shown in Figure 6, respectively. The results demonstrate that the max principal stress appears at the interface of the $P92/Al_2O_3$ for the single-layer coating. The principal stress shows up at the interface between the 8YSZ interlayer and the top $Al_2O_3$ coating for the composite coating system. Therefore, the 8YSZ interlayer could act as a buffer layer between the P92 substrate and the $Al_2O_3$ topcoat, which could effectively reduce thermal stress and improve the thermal cycle endurance of the coating.
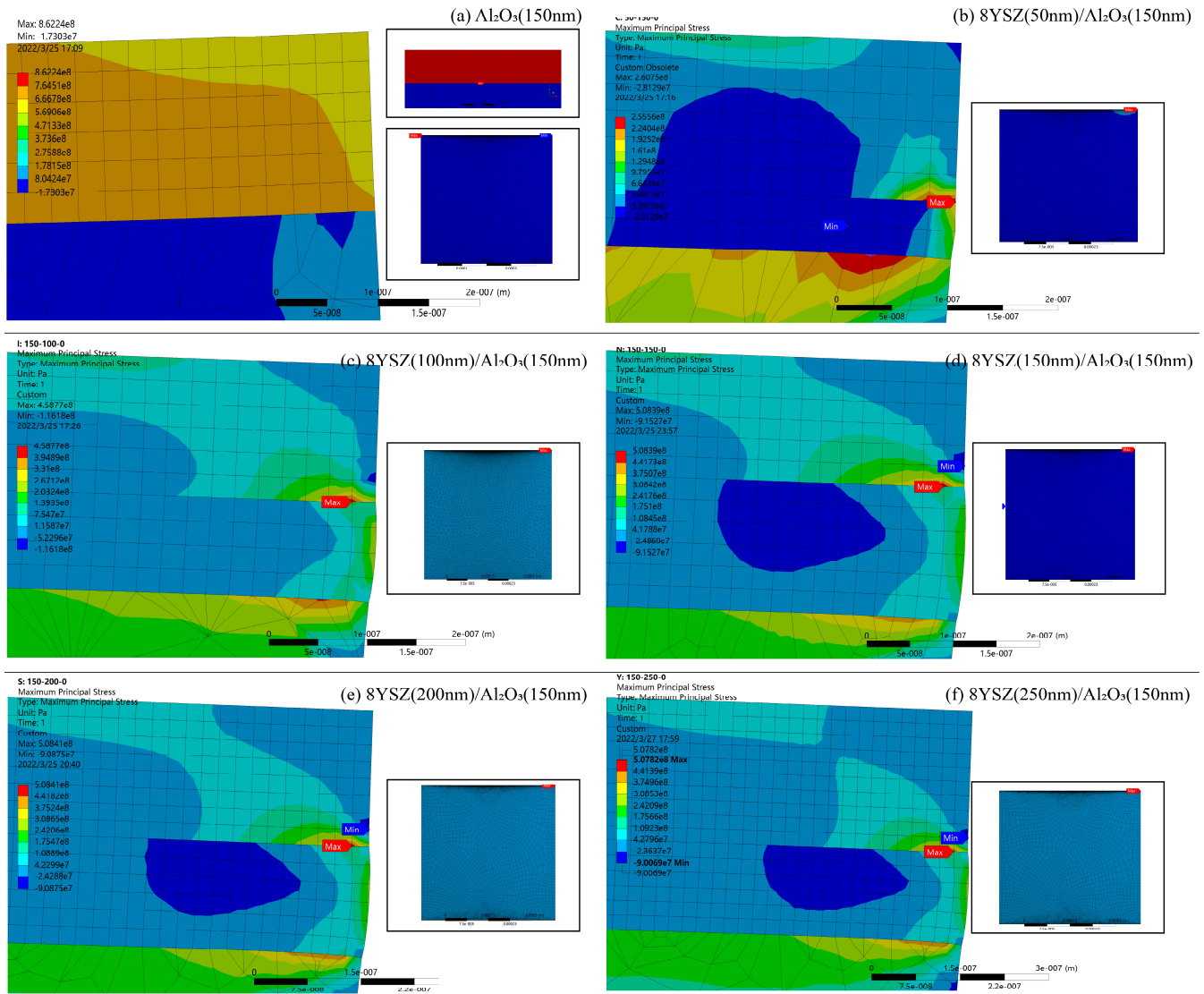


**Figure 6.** Comparison of max principal stress field in $Al_2O_3$ and $8YSZ/Al_2O_3$ coatings, (**a**) $Al_2O_3$ (150 nm); (**b**) 8YSZ (50 nm)/$Al_2O_3$ (150 nm); (**c**) 8YSZ (100 nm)/$Al_2O_3$ (150 nm); (**d**) 8YSZ (150 nm)/$Al_2O_3$ (150 nm); (**e**) 8YSZ (200 nm)/$Al_2O_3$ (150 nm); (**f**) 8YSZ (250 nm)/$Al_2O_3$ (150 nm).

The stress distribution of the two types of coatings is shown in Figure 7. The results show that the stress generally shows similar distribution patterns for each type of coating although the maximum stress values differ. For the single $Al_2O_3$ layer, the distribution of the max principle stress is quite uniform. The principle stress in the top $Al_2O_3$ is generally larger than that in the substrate. Both the maximum shear stress and the maximum mises stress are located at the interface near the edge of the single $Al_2O_3$ layer. When the composite coating is constructed, the maximum principle stress appears at the interface

close to the edge between the top $Al_2O_3$ coating and the 8YSZ interlayer. The maximum shear stress and the maximum mises stress appear at a location similar to that of the max principle stress. The stress distribution changes when the 8YSZ interlayer is placed between the $Al_2O_3$ coating and the P92 substrate as shown in Figure 7. It is observed that the locations of the maximum principal stress, shear stress, and mises stress are shifted to the interface between the top $Al_2O_3$ coating and the 8YSZ coating near the edge. Meanwhile, a large principle stress also appears at the interface of 8YSZ and P95 substrate close to the edge.
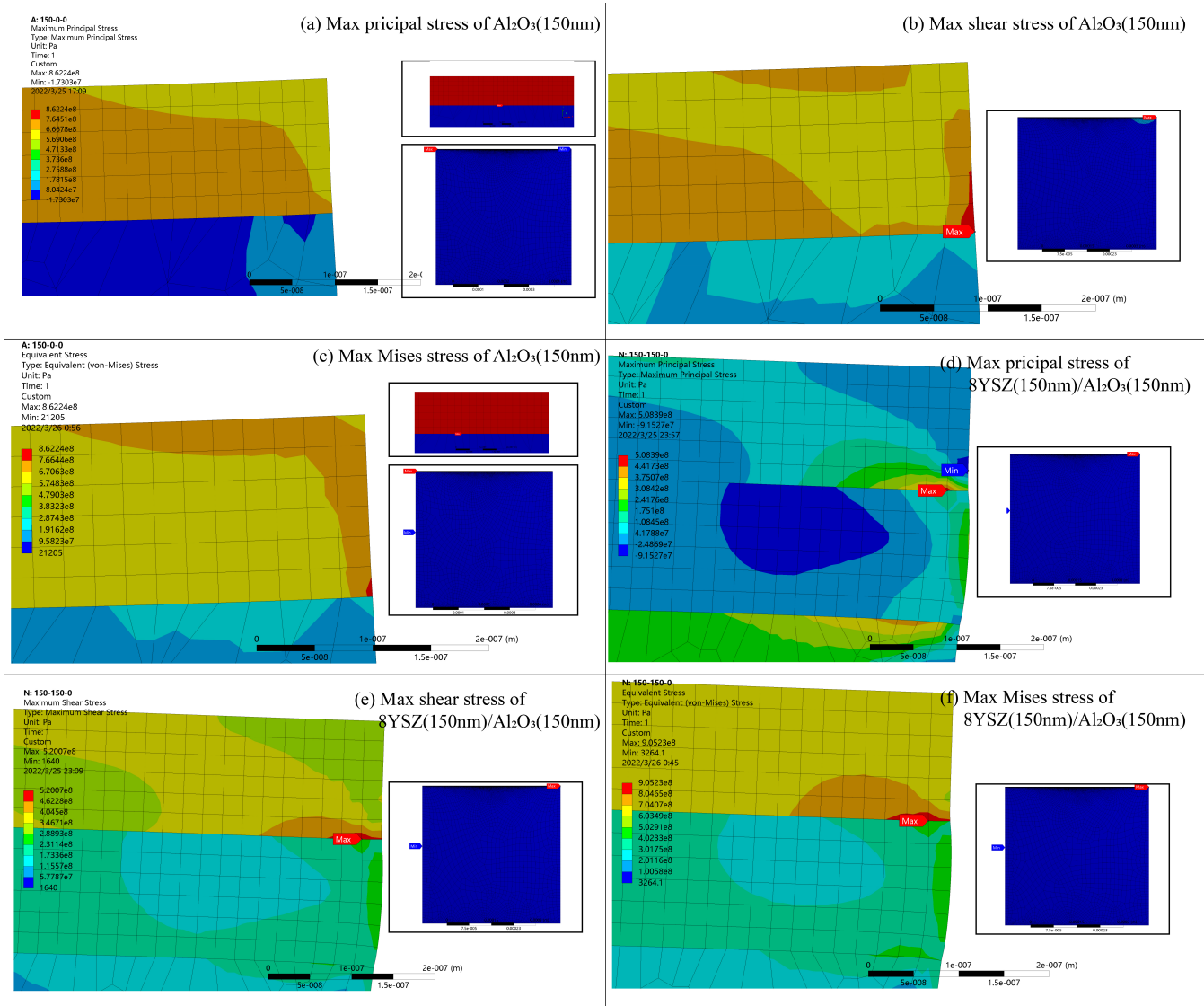


**Figure 7.** Comparison of three kinds of stress distribution, (**a**) Max principal stress, $Al_2O_3$ (150 nm); (**b**) Max shear stress, $Al_2O_3$ (150 nm); (**c**) Max Mises stress, $Al_2O_3$ (150 nm); (**d**) Max principal stress, 8YSZ (150 nm)/$Al_2O_3$ (150 nm); (**e**) Max shear stress, 8YSZ (150 nm)/$Al_2O_3$ (150 nm); (**f**) Max Mises stress, 8YSZ (150 nm)/$Al_2O_3$ (150 nm).

Further analysis of the fracture toughness of single-layer $Al_2O_3$ coating and the 8YSZ/$Al_2O_3$ composite coating are shown in Figure 8. Both $K$ and J-integral are significantly reduced when the 8YSZ interlayer is inserted. Both two values reach the minimum when the 8YSZ layer with a thickness of 100 nm is inserted. The $K_I$ of the 8YSZ (100 nm)/$Al_2O_3$ (150 nm) composite coating is calculated to be 6017.9 Pa·m$^{1/2}$, which is two orders of magnitude lower than that of the mono-layer $Al_2O_3$ coating (159 kPa·m$^{1/2}$). Similarly,

the J-integral of the 8YSZ (100 nm)/$Al_2O_3$ (150 nm) composite coating is calculated to be 0.0023 $J/m^2$, which is two orders of magnitude lower than that of the single-layer $Al_2O_3$ coating, 0.1115 $J/m^2$. When the thickness of the 8YSZ interlayer increases, the $K_I$ and J-integral of the coatings remain almost at a similar level. When the thickness of the interlayer is larger than the stress concentration area around the crack tip, the coating boundary would have little impact on the stress intensity of the crack tip. It could be concluded that inserting an 8YSZ buffer layer could greatly improve the fracture resistance of the $Al_2O_3$ coating, making it more endurable under thermal cycles.
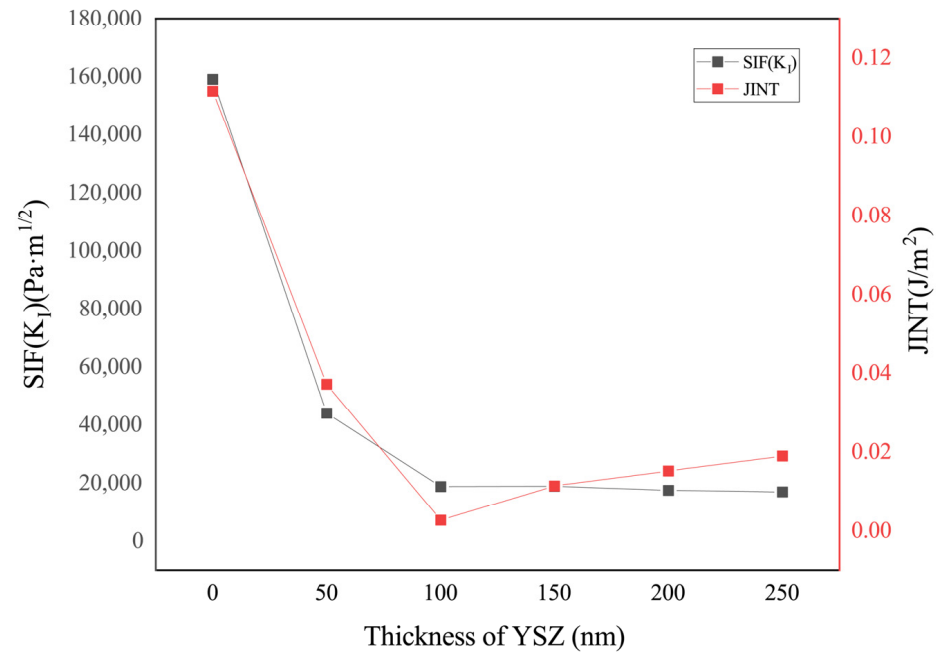


**Figure 8.** Effect of thickness of 8YSZ intermediate layer on the fracture toughness of the system.

The deformation contour of the coating with a pre-meshed crack is shown in Figure 9. The crack propagates from the edge into the coating along the interface of 8YSZ and $Al_2O_3$ coating layers. It was also observed that a minor displacement appears between the 8YSZ and $Al_2O_3$ layers, especially at the coating edge. When the thickness of the 8YSZ buffer layer is less or equal to 150 nm, the buffer layer extrudes out. When the thickness of the buffer layer is greater than 150 nm, the top $Al_2O_3$ layer pops out a little bit and overlaps with the underneath 8YSZ buffer layer, which hence squeezes the crack end together.

The thermal shock experiment was carried out by air cooling the specimens from 700 °C to room temperature (25 °C). The SEM image is shown in Figure 10, in which the micro-crack between the interfaces can be seen in the $P92/Al_2O_3$ specimens. In contrast, no obvious crack was observed in the $P92/8YSZ/Al_2O_3$ specimens which indicates the destruction effect of the thermal stress on the coating was largely reduced. The experiment result agreed with the simulation result that the introduction of an 8YSZ buffer layer could improve the thermal shock endurance of the coating system.
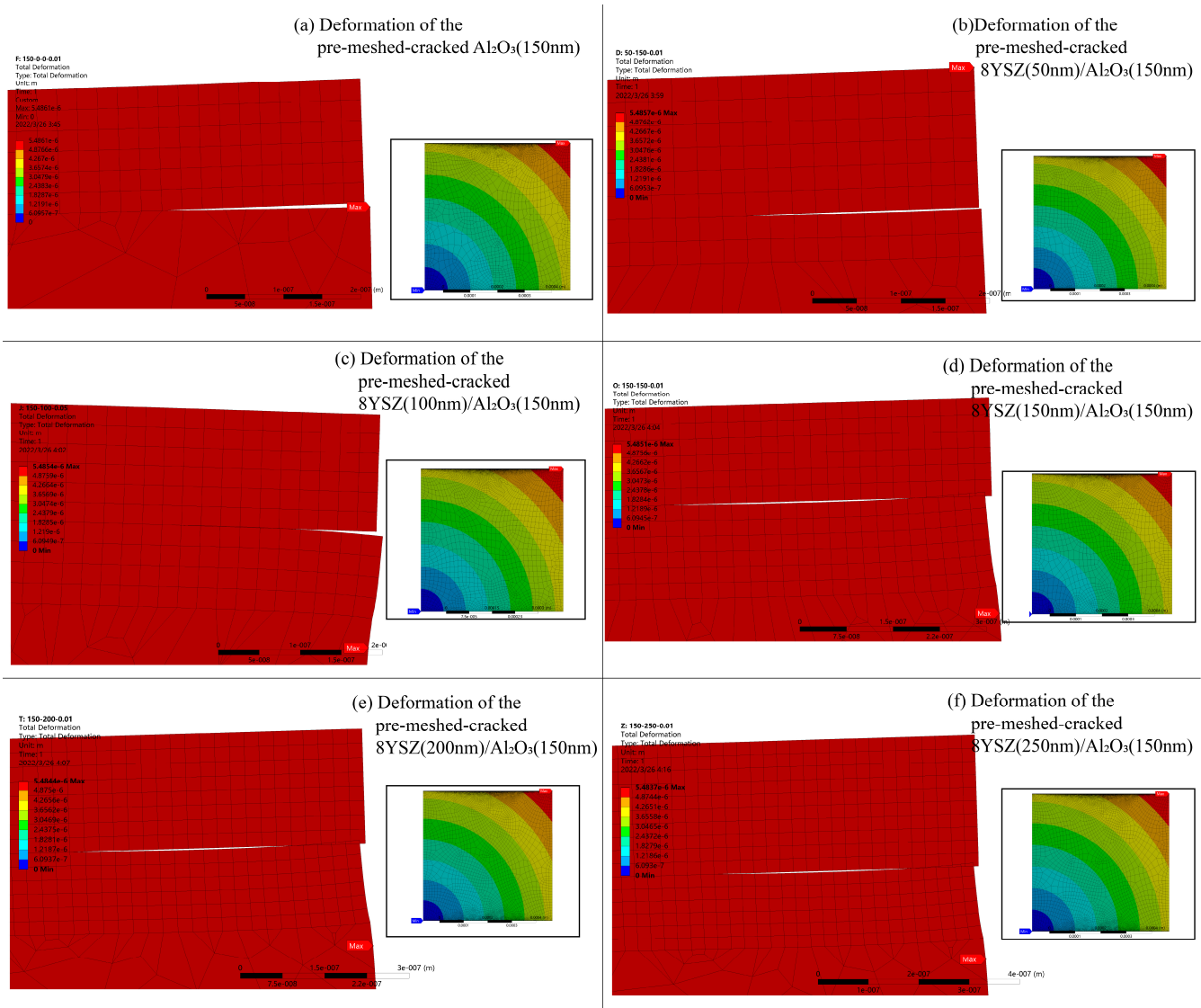
(a) Deformation of the pre-meshed-cracked Al$_2$O$_3$(150nm)

(b) Deformation of the pre-meshed-cracked 8YSZ(50nm)/Al$_2$O$_3$(150nm)

(c) Deformation of the pre-meshed-cracked 8YSZ(100nm)/Al$_2$O$_3$(150nm)

(d) Deformation of the pre-meshed-cracked 8YSZ(150nm)/Al$_2$O$_3$(150nm)

(e) Deformation of the pre-meshed-cracked 8YSZ(200nm)/Al$_2$O$_3$(150nm)

(f) Deformation of the pre-meshed-cracked 8YSZ(250nm)/Al$_2$O$_3$(150nm)

**Figure 9.** The deformation of the models with pre-meshed crack. (**a**) Al$_2$O$_3$ (150 nm); (**b**) 8YSZ (50 nm)/Al$_2$O$_3$ (150 nm); (**c**) 8YSZ (100 nm)/Al$_2$O$_3$ (150 nm); (**d**) 8YSZ (150 nm)/Al$_2$O$_3$ (150 nm); (**e**) 8YSZ (200 nm)/Al$_2$O$_3$ (150 nm); (**f**) 8YSZ (250 nm)/Al$_2$O$_3$ (150 nm).
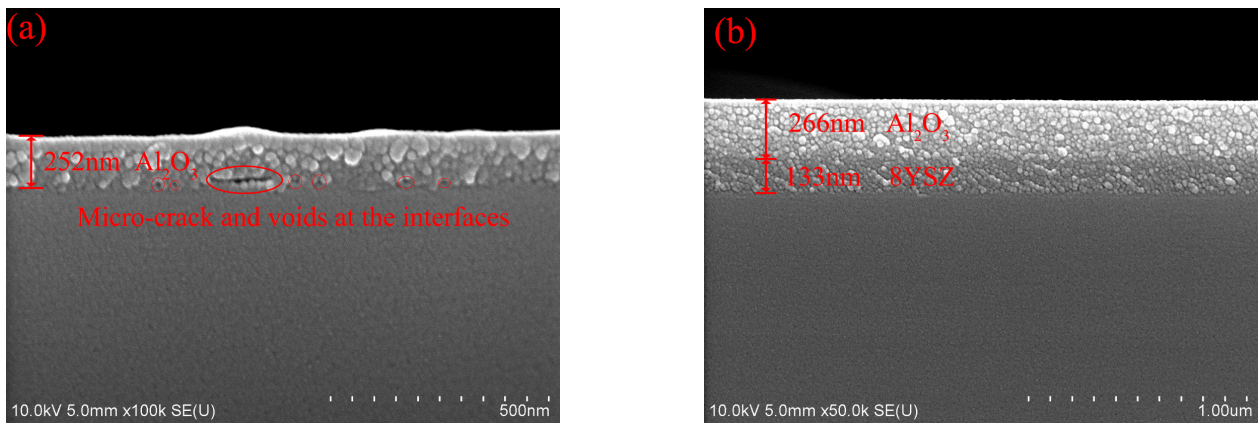
**Figure 10.** The SEM image of specimens after thermal shock test. (**a**) P92/Al$_2$O$_3$ (252 nm); (**b**) P92/8YSZ (155 nm)/Al$_2$O$_3$ (266 nm).

## 4. Conclusions

1.  The 8YSZ buffer layer with proper CTE between the $Al_2O_3$ and P92 and good deformability could relieve local stress concentration and decrease the thermal stress in the coating system.
2.  The 8YSZ buffer layer can significantly reduce the $K_I$ and J-integral by 2 orders of magnitude in the coatings, given the coating system's better crack propagation resistance. The optimal thickness of the 8YSZ buffer layer was 100 nm.
3.  The 8YSZ buffer layer can improve the thermal cycle endurance of the coating system. The P92/8YSZ/$Al_2O_3$ coating system can stay intact without cracking after a thermal shock test, while the P92/$Al_2O_3$ can not.

**Author Contributions:** Methodology, software, formal analysis, original draft preparation, writing—review and editing, K.H.; validation, investigation, visualization, Y.L.; validation, W.W.; Conceptualization, project administration, Q.Y.; funding acquisition, J.M.; project administration, L.H.; supervision, H.L.; formal analysis, B.Y.; resources, W.X.; writing—review and editing, X.C.; data curation, Z.D.; Conceptualization, P.W. All authors have read and agreed to the published version of the manuscript.

**Institutional Review Board Statement:** Not applicable.

**Informed Consent Statement:** Not applicable.

**Data Availability Statement:** The data used to support the findings of this study are included within the article.

**Conflicts of Interest:** Authors Kezhi Huang, Yu Liu, Weijing Wang, Qinghe Yu, Jing Mi, Lei Hao, Hao Liu, Baolong Yuan, were employed by the company, National Engineering Research Center of Nonferrous Metals Materials and Products for New Energy, GRINM Group Co., Ltd and GRIMAT Engineering Institute Co., Ltd. Author Xiao Wei was employed by the company, GRIMAT Engineering Institute Co., Ltd. Author Xiaotao Chen was employed by the company, Shipbuilding Industry Co., Ltd. Author Ping Wang was employed by the company, Zouping Hengjia New Material Technology Co., Ltd.

## References

1.  Bhattacharya, S.P. *Power Generation from Coal*; International Energy Agency (IEA): Paris, France, 2010.
2.  Hasti, S.; Aroonwilas, A.; Veawab, A. Exergy Analysis of Ultra Super-critical Power Plant. *Energy Procedia* **2013**, *37*, 2544–2551. [CrossRef]
3.  Holcomb, G.R. Steam Oxidation and Chromia Evaporation in Ultra-Supercritical Steam Boilers and Turbines. *ECS Trans.* **2009**, *16*, 81–92. [CrossRef]
4.  Basu, S.; Debnath, A.K. *Power Plant Instrumentation and Control Handbook*; Academic Press: Cambridge, MA, USA, 2015; pp. 875–887.
5.  Barnard, P. *Materials for Ultra-Supercritical and Advanced Ultra-Supercritical Power Plants*; Woodhead Publishing: Sawston, UK, 2017; pp. 99–119.
6.  Boissonnet, G.; Bonnet, G.; Pedraza, F. Thermo-Physical Properties of HR3C and P92 Steels at High-Temperature. *J. Mater. Appl.* **2019**, *8*, 59–64. [CrossRef]
7.  Ni, J.; Wang, X.; Gong, J.; Wahab, M.A. Thermal, metallurgical and mechanical analysis of circumferentially multi-pass welded P92 steel pipes. *Int. J. Press. Vessel. Pip.* **2018**, *165*, 164–175. [CrossRef]
8.  Shi, R.-X.; Liu, Z.-D. Hot Deformation Behavior of P92 Steel Used for Ultra-Super-Critical Power Plants. *J. Iron Steel Res. Int.* **2011**, *18*, 53–58. [CrossRef]
9.  El-Magd, E.; Gebhard, J.; Stuhrmann, J. Simulation of the creep behaviour of P92 sandwich structures at 650 °C with loading transverse to the intermediate layer. *Comput. Mater. Sci.* **2007**, *39*, 446–452. [CrossRef]
10. Zhao, L.; Jing, H.; Xu, L.; Han, Y.; Xiu, J. Analysis of creep crack growth behavior of P92 steel welded joint by experiment and numerical simulation. *Mater. Sci. Eng. A* **2012**, *558*, 119–128. [CrossRef]

11. Xu, L.; Liu, S.; Wang, M.; Zhou, S. Crack initiation and propagation mechanism of Al$_2$O$_3$-DBC substrate during thermal cycling test. *Eng. Fail. Anal.* **2020**, *116*, 104720. [CrossRef]

12. Huang, J.; Xie, H.; Luo, L.; Zan, X.; Liu, D.; Wu, Y. Preparation and properties of FeAl/Al$_2$O$_3$ composite tritium permeation barrier coating on surface of 316 L stainless steel. *Surf. Coatings Technol.* **2020**, *383*, 125282. [CrossRef]

13. Yang, H.; Shao, Z.; Wang, W.; Ji, X.; Li, C. A composite coating of GO-Al$_2$O$_3$ for tritium permeation barrier. *Fusion Eng. Des.* **2020**, *156*, 111689. [CrossRef]

14. Liu, Z.; Meng, F.; Yi, L.-B. Simulation of the effects of different substrates, temperature, and substrate roughness on the mechanical properties of Al$_2$O$_3$ coating as tritium penetration barrier. *Nucl. Sci. Tech.* **2019**, *30*, 62. [CrossRef]

15. Wang, W.-J.; Yu, Q.-H.; Liu, X.-P.; Huang, K.-Z.; Mi, J.; Hao, L.; Lu, Z. Microstructure and deuterium resistance of Al$_2$O$_3$/Y$_2$O$_3$ composite coating with different annealing atmospheres. *Rare Met.* **2022**, *41*, 877–882. [CrossRef]

16. Pint, B.; Zhang, Y.; Walker, L.; Wright, I. Long-term performance of aluminide coatings on Fe-base alloys. *Surf. Coatings Technol.* **2007**, *202*, 637–642. [CrossRef]

17. Kuppusamy, M.; Ramanathan, T. Experimental analysis of the thermal-barrier coating for an Al$_2$O$_3$-TiO$_2$ ceramic coated CI engine operating on calophyllum inophyllum oil. *Mater. Teh.* **2021**, *55*, 121–126. [CrossRef]

18. Zhou, C.; Wang, N.; Xu, H. Comparison of thermal cycling behavior of plasma-sprayed nanostructured and traditional thermal barrier coatings. *Mater. Sci. Eng. A* **2007**, *452–453*, 569–574. [CrossRef]

19. Zhang, J.-G.; Tan, X.; Fan, X.-J.; Mao, J.; Deng, C.-M.; Liu, M.; Zhou, K.-S.; Zhang, X.-F. Thermal insulation performance of 7YSZ TBCs adjusted via Al modification. *Rare Met.* **2023**, *42*, 994–1004. [CrossRef]

20. Li, X.-K.; Zhu, S.-P.; Liao, D.; Correia, J.A.; Berto, F.; Wang, Q. Probabilistic fatigue modelling of metallic materials under notch and size effect using the weakest link theory. *Int. J. Fatigue* **2022**, *159*, 106788. [CrossRef]

21. Liao, D.; Zhu, S.-P.; Keshtegar, B.; Qian, G.; Wang, Q. Probabilistic framework for fatigue life assessment of notched components under size effects. *Int. J. Mech. Sci.* **2020**, *181*, 105685. [CrossRef]

22. Wang, W.; Yu, Q.; Liu, X.; Lu, Z. Preparation of Al$_2$O$_3$/Y$_2$O$_3$ composite coating for deuterium permeation reduction. *J. Rare Earths* **2020**, *38*, 1237–1242. [CrossRef]

23. Huang, K.; Wang, W.; Yu, Q.; Hao, L.; Mi, J.; Li, S.; Liu, H.; Li, S.; Liu, J.; Wang, J. Simulation of the Residual Stress of the Y$_2$O$_3$/Al$_2$O$_3$ Composite Deuterium Permeation Barrier under Thermal Shock. *Int. J. Photoenergy* **2021**, *2021*, 6684802. [CrossRef]

24. Lefrou, C.; Nogueira, R.P.; Huet, F.; Takenouti, H. Basic Concepts, High Temperature Corrosion. *Shreir's Corros.* **2010**, *1*, 13–51. [CrossRef]

25. Zhang, X.; Zhang, S. Rethinking the Role That the "Step" in the Load–Displacement Curves Can Play in Measurement Of Fracture Toughness for Hard Coatings. *Thin Solid Films* **2012**, *520*, 3423–3428. [CrossRef]

26. Dillard, D.A. Improving Adhesive Joint Design Using Fracture Mechanics. In *Advances in Structural Adhesive Bonding*; Woodhead Publishing: Sawston, UK, 2010; pp. 350–388. [CrossRef]

27. Qiang, B.; Yong, B. 12-Fatigue and Fracture. In *Subsea Pipeline Design, Analysis, and Installation, Subsea Pipeline Design, Analysis, and Installation*; Gulf Professional Publishing: Houston, TX, USA, 2014; pp. 283–318. [CrossRef]

28. Barmak, K.; Kevin, R.C. *Metallic Films for Electronic, Optical and Magnetic Applications: Structure, Processing and Properties*; Woodhead Publishing: Sawston, UK, 2013; pp. 1–634.

29. Gu, B.; Phelan, P.E. Thermal Peeling Stress Analysis of Thin-Film High-Tc Superconductors. *Appl. Supercond.* **1998**, *6*, 19–29. [CrossRef]